Journal of Computational Physics 474 (2023) 111804

Contents lists available at ScienceDirect

Journal of Computational Physics

journal homepage: www.elsevier.com/locate/jcp

Short note

A short note on a 3D spectral analysis for turbulent flows on unstructured meshes

Panagiotis Tsoutsanis [a,*], Xesus Nogueira [b], Lin Fu [c,d]

[a] Centre for Computational Engineering Sciences, Cranfield University, Cranfield MK43 0AL, United Kingdom
[b] Group of Numerical Methods in Engineering-GMNI, Center for Technological Innovation in Construction and Civil Engineering-CITEEC. Civil Engineering School, Universidade da Coruña, Campus de Elviña, 15071, A Coruña, Spain
[c] Department of Mechanical and Aerospace Engineering, The Hong Kong University of Science and Technology, Clear Water Bay, Kowloon, Hong Kong
[d] Department of Mathematics, The Hong Kong University of Science and Technology, Clear Water Bay, Kowloon, Hong Kong

ARTICLE INFO

Article history:
Received 12 July 2022
Received in revised form 10 October 2022
Accepted 17 November 2022
Available online 23 November 2022

Dataset link: https://doi.org/10.17862/cranfield.rd.21271122

Keywords:
FFT
Unstructured meshes
Implicit large eddy simulation
Turbulent flow
High-order non-linear methods

ABSTRACT

We propose two techniques for computing the energy spectra for 3D unstructured meshes that are consistent across different element types. These techniques can be particularly useful when assessing the dissipation characteristics and the suitability of several popular non-linear high-order methods for implicit large-eddy simulations (iLES). Numerical experiments demonstrate the performance of several element types for iLES of the Taylor-Green vortex, where a significantly different dissipation and dispersion mechanism for each element type is revealed. The energy spectra results are dependent on the technique selected for obtaining them, therefore an additional established technique from the literature is also included for comparison to further analyse their similarities and their differences. These techniques can be an integral tool for the tuning and calibration of non-linear high-order methods that can benefit both explicit and implicit large-eddy simulations (LES).

1. Introduction

Turbulent flows present such a broad range of spatial and temporal scales, that even with today's supercomputers it is not feasible to fully resolve and perform Direct Numerical Simulation (DNS) of practical high-Reynolds (Re) number flows. Large-eddy simulation family of techniques has been established as a high-fidelity method to simulate these flows, by resolving the large-scale flow structures, while the smaller unresolved ones are modelled. An increasing number of approaches [1–9] have resorted to iLES, an approach that employs the unfiltered Navier-Stokes equations while utilising suitable non-linear numerical methods that can implicitly act as a filtering mechanism for the small scales that can not be resolved. Within the iLES context, developing and tuning several sophisticated numerical methods to successfully act as sub-grid-scale (SGS) models at small scales and provide a physically meaningful result, is a formidable task. The main reason is that the "right" amount of numerical dissipation is required, to mimic an SGS model, therefore a numerical method with no dissipation or excessive dissipation is not suitable.

* Corresponding author.
E-mail addresses: panagiotis.tsoutsanis@cranfield.ac.uk (P. Tsoutsanis), xesus.nogueira@udc.es (X. Nogueira), linfu@ust.hk (L. Fu).

https://doi.org/10.1016/j.jcp.2022.111804

High-order non-linear numerical methods have been regularly used for iLES due to their increased accuracy at coarse grid resolutions compared to the standard 2nd-order method, their good parallel performance, and high computational efficiency. High-order methods have also been used for unstructured meshes across several numerical frameworks including finite-volume (FV), and finite-element (FE) discontinuous Galerkin, for iLES of complicated geometries [9–12]. Obtaining analytical expressions for the numerical dissipation and dispersion for several non-linear high-order unstructured-grid-based numerical methods used in iLES is not feasible. Therefore, the developers are relying on utilising canonical well-established test problems (such as the Taylor-Green vortex) with available DNS results, to calibrate the developed methods to exhibit this favourable "right" amount of numerical dissipation. A key performance indicator of these methods is obtained by examining the 3D kinetic energy spectra across several wave numbers to understand if this "right" amount of dissipation is properly reflected by the way that the kinetic energy is dissipated. One technical difficulty of dealing with unstructured meshes for these tests is that the data location of each cell in the unstructured grid is arbitrary/non-uniform and therefore there must be some mapping of non-uniform/arbitrary data to an auxiliary uniform grid to be able to approximate the 3D kinetic energy spectra. This task involves several approximations that should be carefully considered during the interpretation of the obtained results. For unstructured meshes in particular the 3D kinetic energy spectra are frequently neglected in the development and application of high-order methods for iLES due to the aforementioned technical difficulty. This study introduces two techniques that can be used for any high-order numerical methods employing unstructured meshes for obtaining the 3D spectra, and it also compares them with the popular finuFFT [13] technique available. The **UCNS3D** CFD software package [14,15] is employed and the numerical framework is briefly introduced, followed by the methods adopted and numerical experiments using the Taylor-Green vortex with several numerical methods.

2. Numerical framework

Considering a 3D domain Ω consisting of conforming tetrahedral, hexahedral, prism, and pyramid cells, each of which is indexed by a unique mono-index i, the Euler governing equations can be written in a vector form as follows

$$\frac{\partial}{\partial t}\int_{V_i}\mathbf{U}\,dV+\int_{\partial V_i}\mathbf{F}_n\,dS=0, \tag{1}$$

where $\mathbf{U}=\mathbf{U}(\mathbf{x},t)$ is the vector of conserved variables and, $\mathbf{F}_n$ is the non-linear flux in the direction normal to the cells interface as given below

$$\mathbf{U}=\begin{bmatrix}\rho\\ \rho u\\ \rho v\\ \rho w\\ E\end{bmatrix},\mathbf{F}_n=\begin{bmatrix}\rho u_n\\ \rho u u_n+n_x p\\ \rho v u_n+n_y p\\ \rho w u_n+n_z p\\ u_n(E+p)\end{bmatrix}, \tag{2}$$

where u_n is the velocity normal to the bounded surface area, defined by $u_n=n_x u+n_y v+n_z w$. The total energy $E=\rho e+0.5\rho(u^2+v^2+w^2)$, with the internal energy being $e=p(\gamma-1)^{-1}\rho^{-1}$, pressure p and γ the gas constant. Integrating Eq. (1) over a mesh element i using a high-order explicit finite-volume formulation, the following equation is obtained as

$$\frac{d\mathbf{U}_i}{dt}=\frac{1}{|V_i|}\sum_{j=1}^{N_f}\sum_{\alpha=1}^{N_{qp}}\left(F_{\mathbf{n_{ij}}}\left(\mathbf{U}^n_{ij,L}(\mathbf{x}_{ij,\alpha},t),\mathbf{U}^n_{ij,R}(\mathbf{x}_{ij,\alpha},t)\right)\right)\omega_\alpha|S_{ij}|, \tag{3}$$

where $\mathbf{U}_i$ is the volume averaged vector of variables

$$\mathbf{U}_i=\frac{1}{|V_i|}\int_{V_i}\mathbf{U}(x,y,z)\,dV, \tag{4}$$

and $F_{\mathbf{n_{ij}}}$ is a numerical flux function in the direction normal to the cell interface between a considered cell i and one of its neighbouring cells j. N_f is the number of faces per element, N_{qp} is the number of quadrature points used for approximating the surface integrals, $|S_{ij}|$ is the surface area of the corresponding face, and $\mathbf{U}^n_{ij,L}(\mathbf{x}_{ij,\alpha},t)$ and $\mathbf{U}^n_{ij,R}(\mathbf{x}_{ij,\alpha},t)$ are the high-order approximations of the solutions for cell i and cell j respectively. α corresponds to different Gaussian integration points $\mathbf{x}_\alpha$ and weights ω_α over each face. $\mathbf{a}^n_{i,1}$ corresponds to the volume averaged volume fraction of cell i at time level n. The volume, surface and line integrals are numerically approximated by a suitable Gauss-Legendre quadrature. The reconstruction is based on the previous work of Tsoutsanis et al. [16,17] and Tsoutsanis and Dumbser [9], where the readers are referred for further details, and two types of schemes are employed in this study, i.e., the central 3rd- and 5th-order linear schemes, and the Central Weighted Essentially Non-Oscillatory (CWENO) schemes with the 3rd- and 5th-order of spatial accuracy.

For the inviscid fluxes, the approximate HLLC (Harten-Lax-van Leer-Contact) Riemann solver of Toro [18] is employed and the temporal discretisation employs the 4^{th}-order explicit Strong Stability Preserving (SSP) Runge-Kutta method [19], which

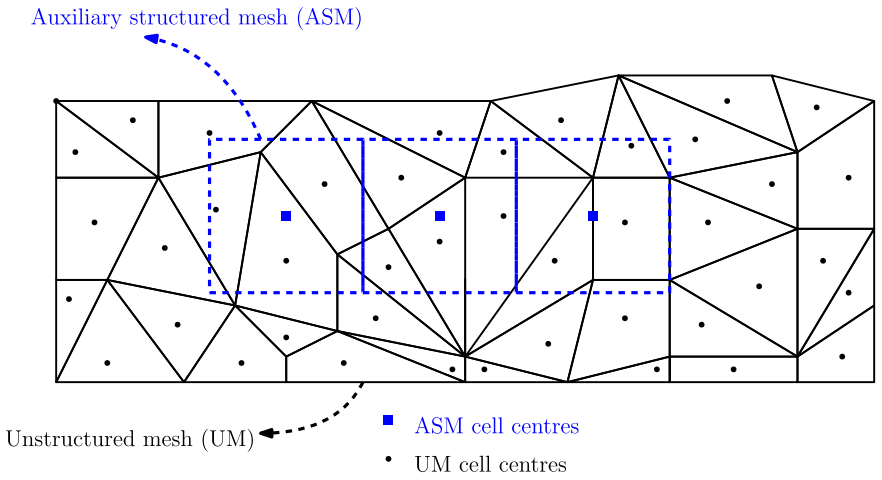

Fig. 1. Drawing of 2D Unstructured mesh and the ASM arrangement.

is stable for $CFL \approx 1.5$. All the schemes employed are implemented in the well established over several test problems [20–28] open-source **UCNS3D** CFD code [14,15]. It has been developed using object-oriented Fortran 2003, MPI message passing interface (MPI), and the Open Multi-Processing (OpenMP) application programming interface (API). The reader is referred to [10,15,29] for more details on implementation and performance benchmarks.

3. 3D spectra methodology

The techniques developed for ensuring a unified and transparent spectra analysis across different mesh types and element types, follow in principle the established FFT [30] techniques for Cartesian meshes, but adapted to unstructured meshes. The primary goal is to transfer the quantity of interest Q (such as kinetic energy) from an unstructured mesh to a 3D auxiliary structured mesh (ASM) of similar grid resolution and then perform the FFT. To better understand the challenges associated with this goal, consider the drawing of a 2D unstructured mesh and its corresponding auxiliary 2D structured mesh as shown in Fig. 1. From this arrangement, it can be realized that:

1. There are unstructured mesh elements that only a portion of them lies within the (ASM) element of similar resolution.
2. There are ASM elements that might include the cell-centres of more than one unstructured element.
3. In extreme cases there might be ASM elements that might not include any cell-centre of an unstructured element.

Therefore these occurrences must be taken under consideration when developing a technique to map unstructured mesh data to ASM.

3.1. `Method 1`

The first method that we are proposing is to perform an average of the quantity of interest of all the unstructured elements whose cell-centre or any vertex lies within the area/volume of the ASM element considered as follows:

1. Identify all the unstructured mesh elements whose cell-centres lie within the volume region occupied by each ASM element as shown in Fig. 2. If we encounter the extreme case where none of the cell-centres lies within then we look at the vertices of the elements that might lie within the volume region.
2. Perform a simple average of the solutions of the unstructured elements to their corresponding element of the ASM as shown below

$$Q^{ASM}_{(i,j,k)} = \frac{\sum_{j=1}^{N} Q_j}{N}, \tag{5}$$

   where N is the number of elements satisfying the above criterion, and $Q^{ASM}_{(i,j,k)}$ being the computed averaged quantity of interest, at the ASM element at location (i, j, k)
3. Once the quantity of interest Q has been computed for each element of the ASM then perform the FFT.

In idealized situations, the total volume of the elements satisfying the criterion for `Method 1`, will be exactly the same as the volume of the corresponding ASM element, as shown in Fig. 3.

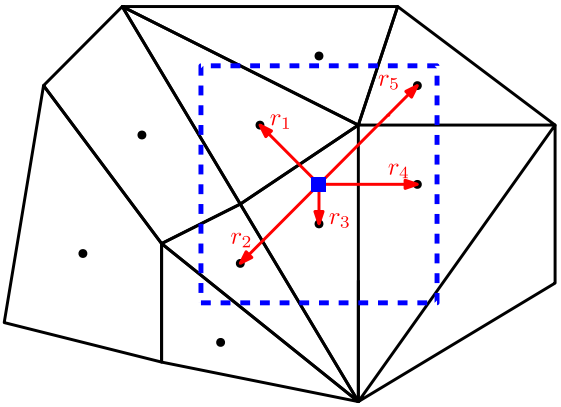

Fig. 2. Drawing of 2D Unstructured mesh elements and a single ASM element arrangement.

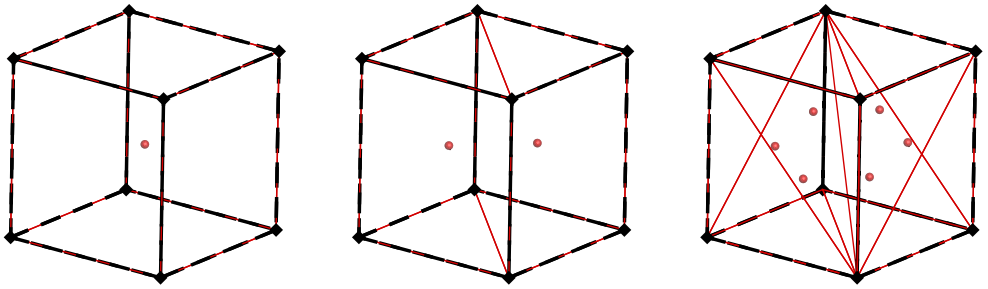

(a) hexa (b) prism (c) tetra

Fig. 3. Hexahedral (left), prismatic (middle), and tetrahedral (right) cells edges indicated by red colour, their corresponding cell centres illustrated by red spheres, and their ASM element edges indicated by dashed black coloured lines. (For interpretation of the colours in the figure(s), the reader is referred to the web version of this article.)

3.2. Method 2

The second method that we are proposing is to assign the quantity of interest equal to that of the unstructured element whose cell centre is closest to the cell centre of the considered ASM element as follows:

1. Identify which of the unstructured mesh element cell-centres is closer to the cell-centre of the considered ASM element as shown in Fig. 2, where the unstructured mesh element with the distance r_3 is the closest. If we encounter the extreme case where none of the cell-centres lies within then we look at the vertices of the elements that might lie within the volume region and their corresponding distance from the cell centre of the ASM element.
2. Assign the solution of the considered ASM equal to the unstructured mesh element previously identified

$$Q^{ASM}_{(i,j,k)} = Q_j, \qquad \text{Unstructured element j is the closest}, \tag{6}$$

   and $Q^{ASM}_{(i,j,k)}$ being the computed quantity of interest, at the ASM element at location (i, j, k)
3. Once the quantity of interest Q has been computed for each element of the ASM then perform the FFT.

It needs to be stressed that the postprocessing error associated with this method cannot be easily quantified, since the closest neighbouring cell will be selected as shown in Fig. 2 with distance r_3 from the cell-centre of the corresponding ASM cell, while the rest of the computational cells will be neglected. On a first read, neglecting these elements might imply that modes that might be present in these cells are completely missed, however, the employed multidimensional reconstruction finite-volume method uses several stencils [31] which include all of the cells within the close vicinity and therefore it takes their values into account implicitly.

3.3. Method 3

The third method that we will be employing for comparison purposes is the recently established finuFFT [13] technique available, which is based upon the “exponential semicircle” kernel. One key characteristic of this approach that should be

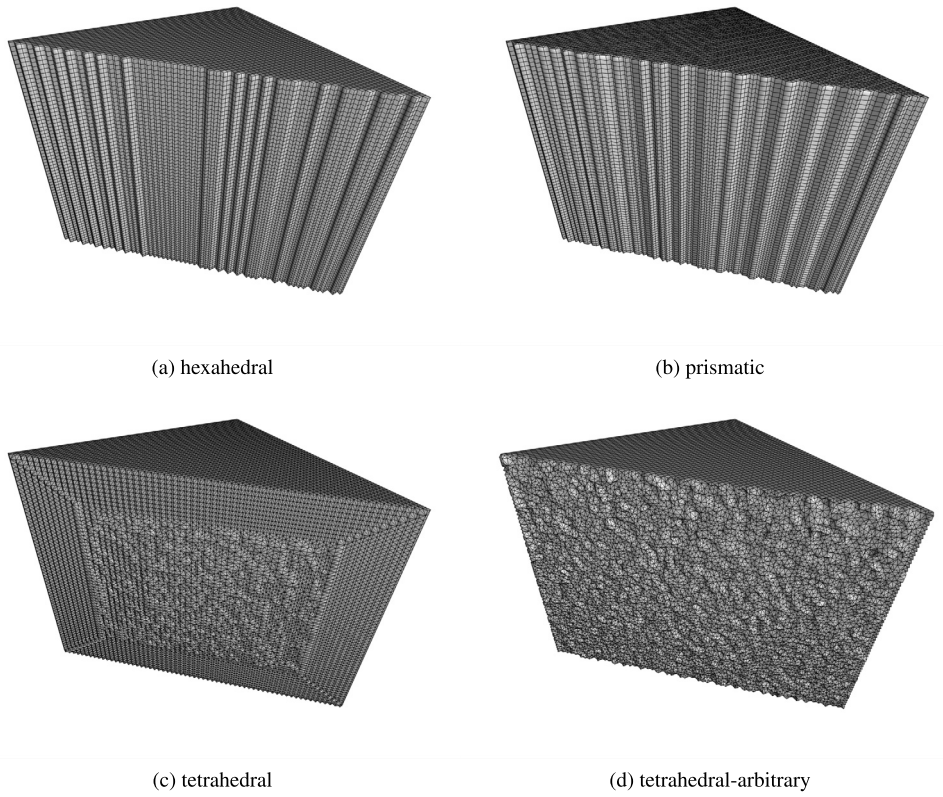

Fig. 4. Cutaway sections of the unstructured meshes used for the Taylor-Green vortex flow test problem. A hexahedral, prismatic, purely tetrahedral, and an arbitrary tetrahedral-dominant mesh are depicted from left to right respectively.

taken into consideration is that the non-uniform to the uniform type of interpolation involves the transfer of the solution to a finer mesh (upsampling), performing the FFT, and then performing a roll-off correction or deconvolution on the corresponding mesh resolution of the ASM. The readers are referred to [13] for details of the technique. In this work we have performed the computations with this method using the code that the authors of [13] have developed and made freely available in [32]. In particular, we have used the finufft3d1 subroutine, which performs a 3D complex nonuniform FFT of type 1 (nonuniform to uniform). More detailed analysis of the parameters influencing the performance of finufft3d1, such as the tolerance used, is not pursued in this study, but it might reveal some additional characteristics of this method and it is worth pursuing in the future. Here, we have used the default value of the parameters.

As it can be realized from Fig. 2, there is an overwhelming number of possibilities that could be explored for mapping the solution from the unstructured mesh to the ASM, including interpolation techniques such as least-squares, and weighted least-squares that can already be available in unstructured finite-volume CFD solvers. However the main goal of this study is firstly to introduce two simple cost-efficient techniques that can be applied to unstructured mesh solvers across several frameworks, secondly compare their performance against a well-established technique of finuFFT [13], and finally, to understand how the influential the technique selected is in the interpretation of 3D kinetic energy spectra.

4. iLES of Taylor-Green vortex

The iLES of the 3D inviscid Taylor-Green vortex test problem is employed, for assessing firstly the performance of four different types of meshes (hexahedral, prismatic, tetrahedral, and arbitrary tetrahedral mesh) and secondly two classes of schemes (central and CWENO) schemes. This test aims to examine the ability of a numerical method to reproduce the transition to turbulence. It is a widely used problem for the assessment of the performance of numerical methods within the LES context and in particularly for "under-resolved" mesh resolutions [4,6,9,25,26,31,33–36]. The computational domain is defined as $\Omega = [0, 2\pi]^3$ with periodic boundary conditions. The reader is referred to [6,33,34] for the details of the initial conditions.

The initial condition corresponds to an initial Mach number $M \approx 0.08$, with wavenumber $k = 2\pi/\lambda = 1$. Simulations were carried out on a hexahedral, prismatic, purely tetrahedral and an arbitrary tetrahedral-dominant (included pyramids at periodic boundaries) mesh with a cell edge resolution equivalent to 64^3 as shown in Fig. 4. The chosen hexahedral mesh consists of elements of equal size and uniform spacing throughout, and therefore corresponds to a purely cartesian/structured mesh. The rationale behind this choice is so that all the different methods could be tested to ensure that they provide

Table 1
Mesh characteristics for Taylor-Green vortex test problem.

mesh type	edges per domain Length L	Total number of cells
hexahedral	64	262,144
prismatic	64	524,288
uniform tetrahedral	64	1,572,864
arbitrary tetrahedral	64	2,013,134

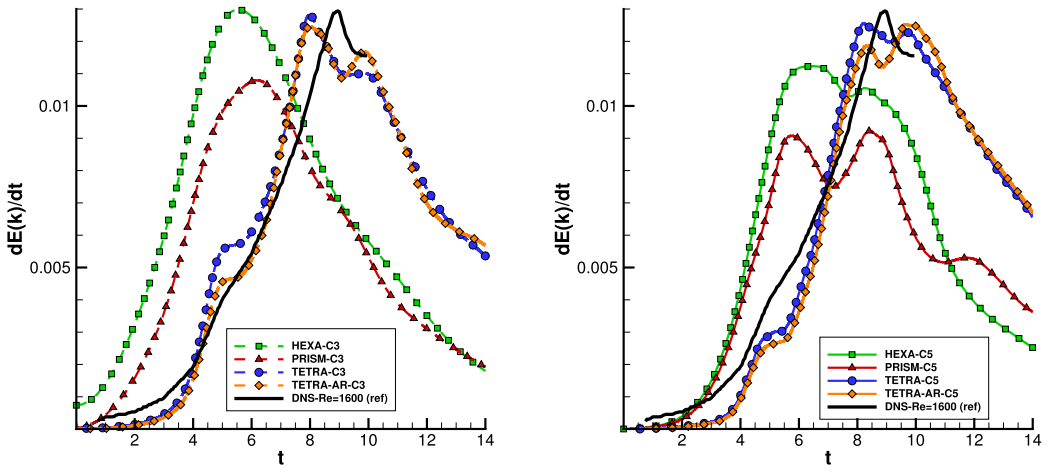

(a) 3rd-order central method (b) 5th-order central method

Fig. 5. Time evolution of kinetic energy dissipation rate for the solution of the Taylor-Green vortex computed with a central 3rd-order scheme (C3) and a central 5th-order scheme (C5) scheme on several unstructured meshes with a cell edge resolution equivalent to 64^3. It can be noticed that tetrahedral meshes exhibit the closest agreement with the reference DNS results of Brachet [44] followed by the prismatic and hexahedral mesh.

the same results by using a mesh that matches exactly the ASM. Four different types of meshes are used namely hexahedral, prismatic, uniform tetrahedral, and arbitrary tetrahedral consisting of their specifications as detailed in Table 1. In our approach, the four meshes selected have an equivalent resolution in terms of their element edge (h), although each of them has a different number of cells. Alternatively, one could have selected four meshes with a similar number of cells but that would translate to a significantly different edge resolution (h) between them. Both approaches could be viewed as valid, but we have chosen to focus on the edge resolution since our reconstruction polynomials include terms related to $(h, h^2, h^3, ...)$ which is the approach most commonly used in the literature as seen in [9,12,37–43]. The chosen resolution is such that the total number of cells for each mesh are going to be different, but their element edge resolution (h) is approximately the same, but this approach is sufficient for comparing unstructured meshes of similar resolution for the purpose of this study. It needs to be stressed that the three (hexahedral, tetrahedral, and prismatic) out of the four meshes satisfy the condition that the total sum of the volume of the N elements is exactly equal to the volume of each corresponding element from the ASM. However, the number of degrees of freedom of each grid is different. The central and CWENO schemes were used with a CFL number of 1.3 for the explicit Runge-Kutta 4th-order scheme, up to $t = 14$ for obtaining the dissipation statistics.

From the time evolution of the kinetic energy dissipation rate as seen in Fig. 5, it can be noticed that the tetrahedral meshes provide the closest agreement with the DNS reference results of [44], as opposed to the prismatic and hexahedral mesh. It must be highlighted that the dominant double-peak structure observed with the 5th-order central scheme, has been previously associated with dispersive properties of the numerical methods in several studies [6,9]. One could easily assume that this result is expected because there are more tetrahedral elements in the mesh compared to the hexahedral and prismatic mesh. However, this is not the primary reason, since it has been previously documented [26] that the arbitrary orientation of tetrahedral elements is the key-contributor to significantly lower dissipation errors compared to hexahedral elements. In that previous work [26], it is also demonstrated (Fig. 29 and Fig 30 of this reference) that even a tetrahedral mesh of 32^3, can resolve more features and is less dissipative than a 64^3 hexahedral mesh containing more elements, unless a low-Mach number correction is applied for the hexahedral meshes. The reader is referred to [26] for a detailed description of these behaviours.

We are particularly interested in the 3D spectra of the kinetic energy after the dissipation peak ($t = 10$), where we can assess if the dissipation follows the behaviour of Kolmogorov's (k=-5/3) law, at least for a limited range of wave numbers as expected for the under-resolved resolution employed in this study.

Initially we employ the central 5th-order scheme (C5) scheme with the hexahedral mesh which is uniform and matches exactly the ASM mesh with the three methods. All the methods should produce the exactly same result, and as expected,

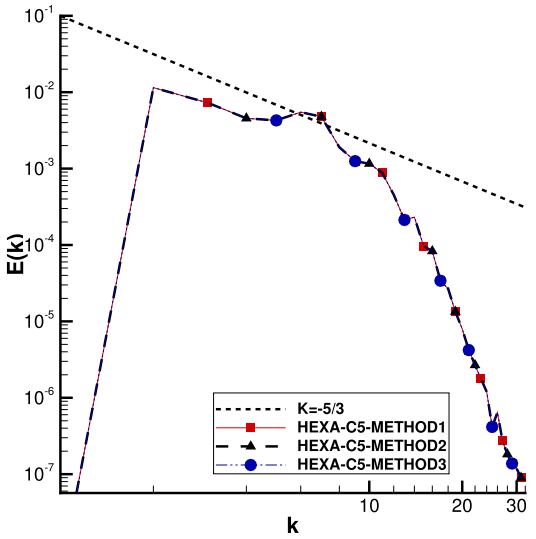

Fig. 6. Kinetic energy 3D spectra at $t = 10$ for the solution of the Taylor-Green vortex computed with a central 5th-order scheme (C5) scheme on hexahedral mesh with a cell edge resolution equivalent to 64^3 obtained with all the methods. It can be noticed that all the methods produce exactly the same result as expected.

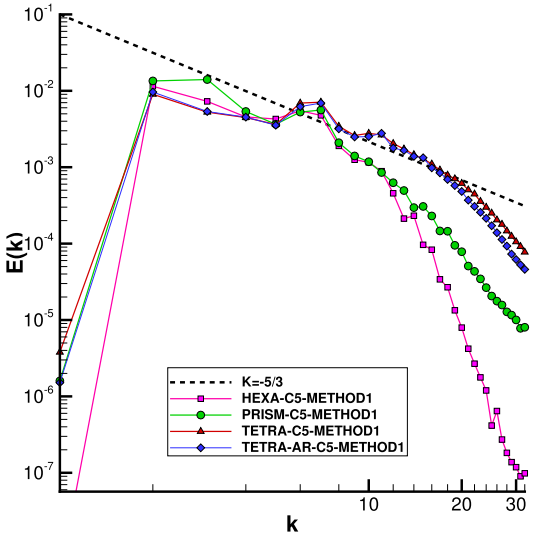

Fig. 7. Kinetic energy 3D spectra at $t = 10$ for the solution of the Taylor-Green vortex computed with a central 5th-order scheme (C5) scheme on several unstructured meshes with a cell edge resolution equivalent to 64^3 obtained with `Method 1`. It can be noticed that tetrahedral meshes exhibit the smallest dissipation followed by the prismatic and hexahedral mesh.

all of them do, as can be seen in Fig. 6. We need to stress that the primary motivation for this particular test is to separate the error of the scheme from the error of the post-processing, and all the methods exhibit the exact same results in this uniform mesh, which implies that the post-processing error is the same for all of the methods and that we can truly appreciate the error of the scheme. However, for unstructured meshes, this is not possible, and recent comprehensive studies on dispersion-dissipation relationships have highlighted that even when employing approximate dispersion relations for 2D and 3D unstructured meshes, and even for linear schemes, it may lead to results that are not understandable and therefore of unclear value at present [45].

Employing `Method 1` and the Central 5th-order scheme for obtaining the kinetic energy 3D spectra at $t = 10$ it can be initially noticed that tetrahedral meshes exhibit the smallest dissipation and therefore have the closest agreement with Kolmogorov's theoretical behaviour for the largest range of wave numbers followed by the prismatic and hexahedral mesh as shown in Fig. 7.

Since there is a perfect mapping between the hexahedral mesh and the ASM, we now focus on comparing the obtained 3D spectra with the different methods on the other types of meshes. We examine firstly the differences between the three

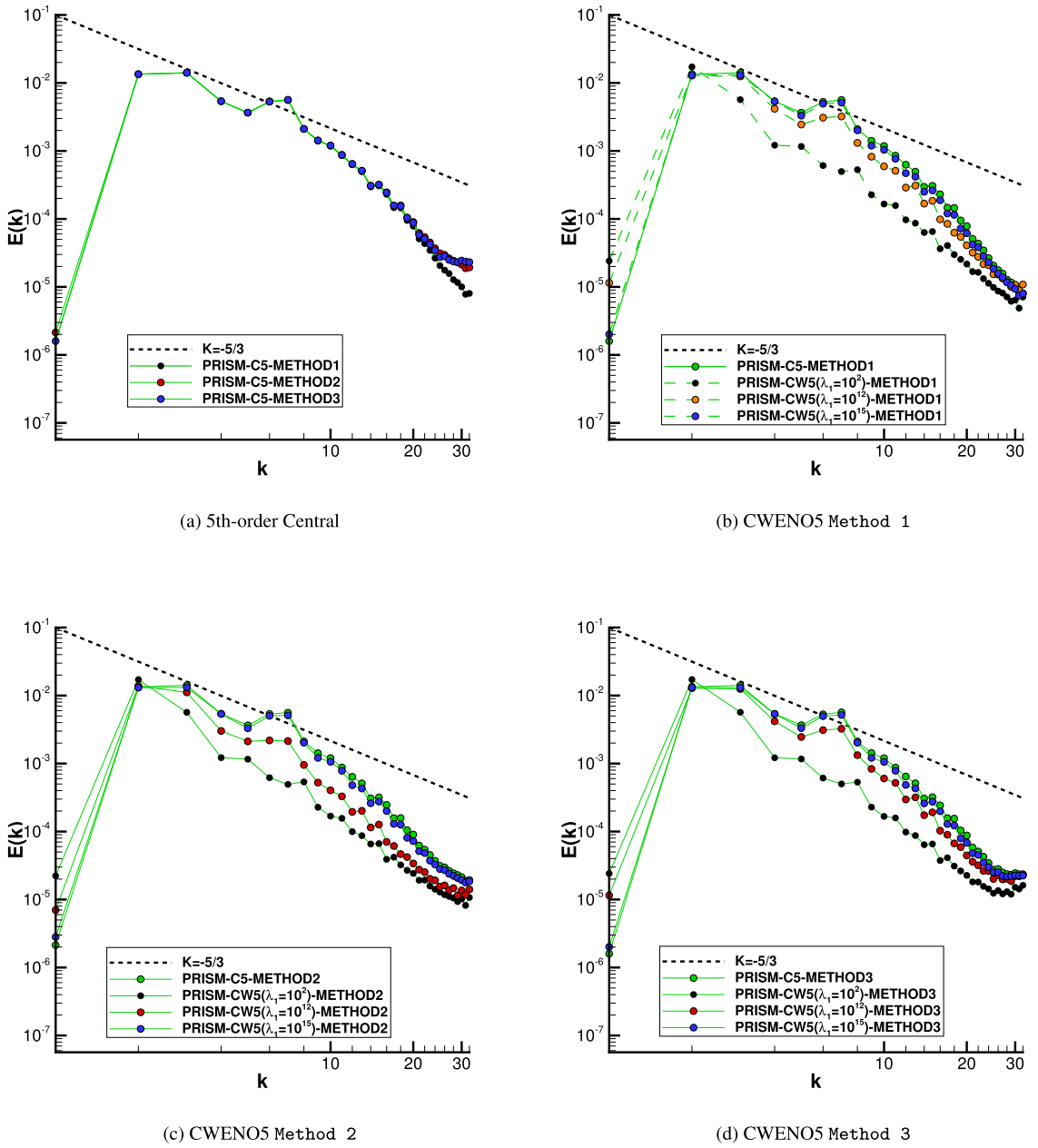

(a) 5th-order Central

(b) CWENO5 `Method 1`

(c) CWENO5 `Method 2`

(d) CWENO5 `Method 3`

Fig. 8. Kinetic energy 3D spectra at $t = 10$ for the solution of the Taylor-Green vortex computed with a central 5th-order scheme (C5) scheme and CWENO5 schemes with different central stencil weights obtained with different methods on prismatic mesh with a cell edge resolution equivalent to 64^3. It can be noticed that lower values of central stencil linear weight λ_1 increases the dissipation for the CWENO 5th-order scheme and `Method 2` and `Method 3` provide the least dissipative behaviour, followed by `Method 1`.

methods using a Central 5th-order scheme, and secondly the influence of the central stencil linear weight λ_1 for the CWENO 5th-order scheme. A very large value of λ_1 translates to smaller dissipation since the central stencil has the largest influence in smooth regions of the flow and eventually resembles more the central 5th-order scheme, while a lower value translates to a more dissipative method that resembles more a 2nd-order upwind method as reported by Tsoutsanis and Dumbser [9], where the reader is referred for more details for the present implementation. Therefore we ultimately want to understand how this change in the dissipation characteristics of the CWENO method is reflected on each type of mesh, and for each method used to obtain the 3D spectra.

Starting with the prismatic mesh results as shown in Fig. 8 when using a Central 5th-order scheme, the similarities across the different methods end at high-wave numbers ($k > 20$), where `Method 1` provides the most dissipative behaviour at high-wave numbers which is indicative of the averaging process employed in this context which acts as a filtering

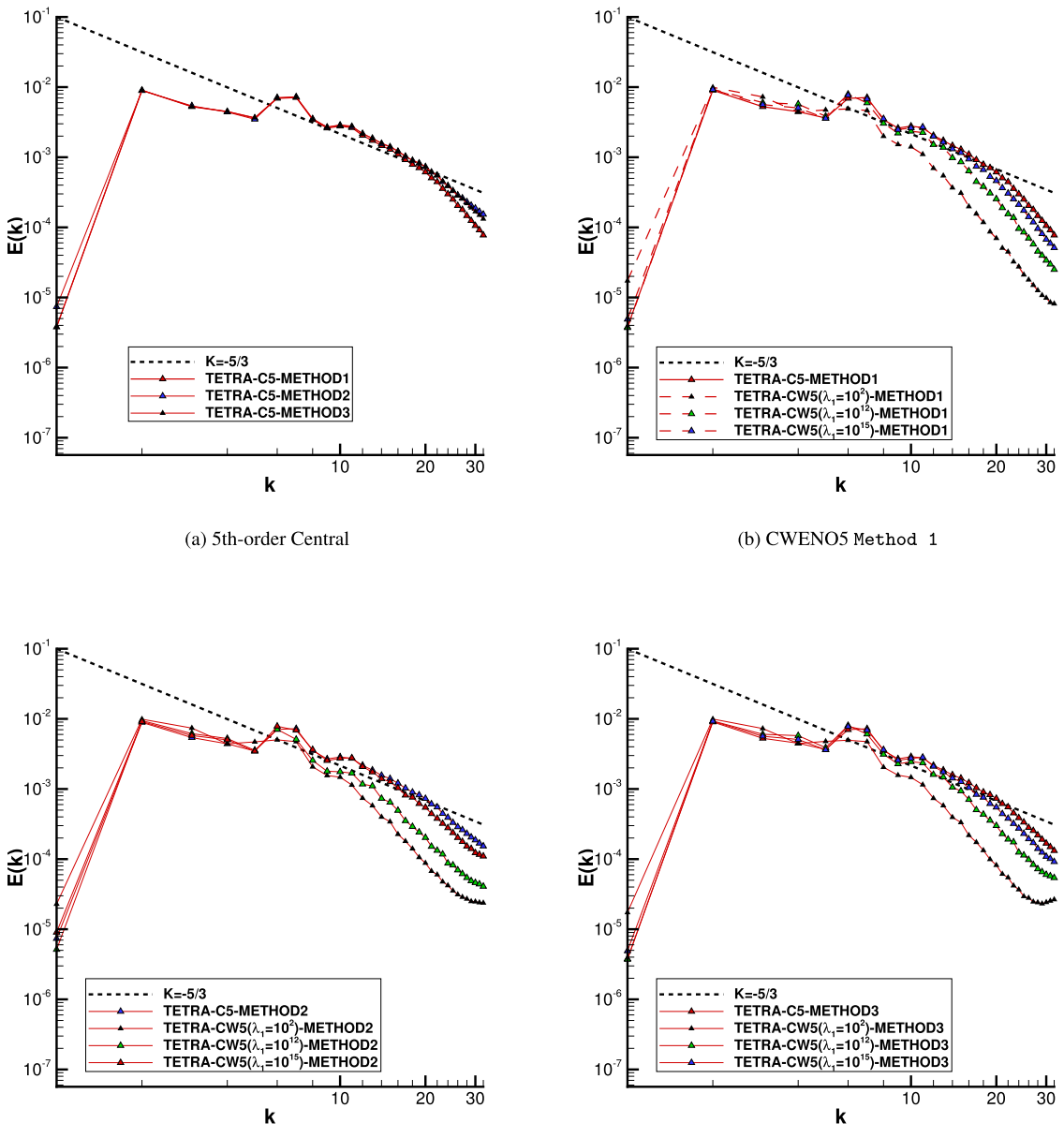

(a) 5th-order Central

(b) CWENO5 `Method 1`

(c) CWENO5 `Method 2`

(d) CWENO5 `Method 3`

Fig. 9. Kinetic energy 3D spectra at $t = 10$ for the solution of the Taylor-Green vortex computed with a central 5th-order scheme (C5) scheme and CWENO5 schemes with different central stencil weights obtained with different methods on tetrahedral mesh with a cell edge resolution equivalent to 64^3. It can be noticed that with `Method 2` and `Method 3` a wider range of scales is resolved compared to `Method 1` for the central scheme, while the `Method 1` provides the most dissipative results.

mechanism. The `Method 2` on the other hand by using the closest neighbour values -that are computed by a high-order reconstruction that takes into account the values of all the elements in the stencils- provides results that exhibit less dissipation and a more desirable slope for high-wave numbers as well and are in good agreement with `Method 3` that is based on the finufft [13] algorithm. When looking at the CWENO 5th-order results, where it is previously documented [9] that low values of λ_1 increase dissipation `Method 3` tails-off at higher frequencies slightly earlier than `Method 2` and therefore this needs to be further investigated for the other meshes.

For the tetrahedral mesh results as shown in Fig. 9 when using a Central 5th-order scheme, the similarities between the different methods are greater compared to the prismatic mesh. Similarly as before the `Method 1` provides the most dissipative behaviour at high-wave numbers, and the `Method 2` and `Method 3` provide results that exhibit less dissipation and a better agreement with the Kolmogorov's slope and are quite similar to each other even at high frequencies. Examining

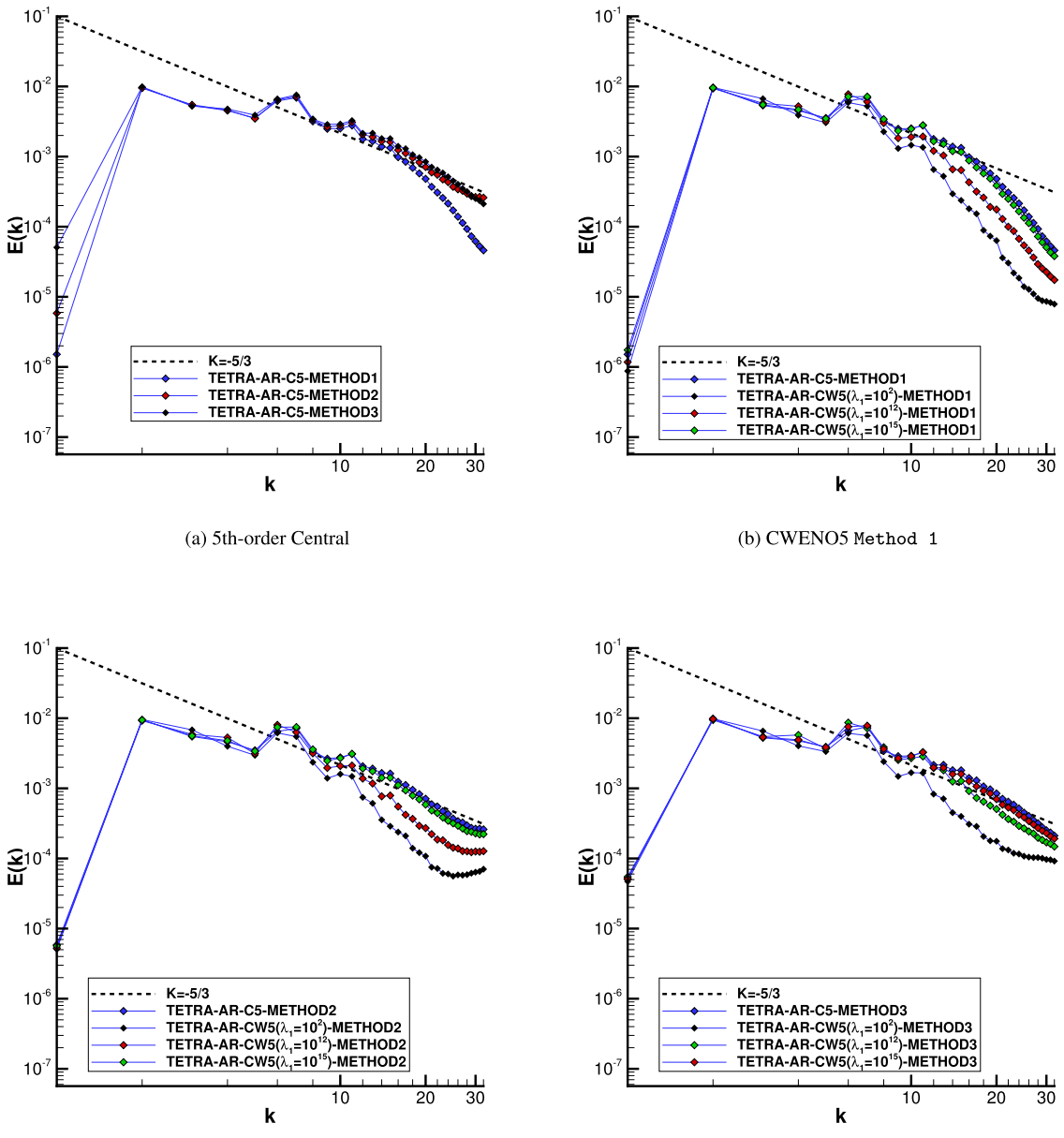

(a) 5th-order Central

(b) CWENO5 `Method 1`

(c) CWENO5 `Method 2`

(d) CWENO5 `Method 3`

Fig. 10. Kinetic energy 3D spectra at $t = 10$ for the solution of the Taylor-Green vortex computed with a central 5th-order scheme (C5) scheme and CWENO5 schemes with different central stencil weights obtained with different methods on tetrahedral-arbitrary mesh with a cell edge resolution equivalent to 64^3. It can be seen that a wider range of wave numbers is captured with this mesh compared to the other ones, and a better agreement with the Kolmogorov's slope is attained. `Method 2` and `Method 3` technique provides the closest agreement with the Kolmogorov's slope for low-dissipation variants of the CWENO5 schemes.

the behaviour of the methods at the CWENO 5th-order results, a sightly more pronounced tail-off is observed for `Method 3` compared to `Method 2` as the dissipation increases (and the central stencil linear weight decreases), where the `Method 1` provides similar behaviour as before. This behaviour can be attributed to under-sampling for the high frequencies of `Method 3` or the missing of some of the content from `Method 2` due to the nearest neighbour strategy used.

Finally for the arbitrary tetrahedral mesh results as shown in Fig. 10 there is a significant difference between the averaging employed for `Method 1` from `Method 2` and `Method 3` that are quite similar for the Central 5th-order scheme. Interestingly enough both `Method 2` and `Method 3` exhibit a tail-off for the CWENO5 method with low central stencil weight values, and it is slightly more pronounced for `Method 2`. This is the mesh that due to its arbitrariness, the variation of the number of cells contained within the volume of the corresponding ASM can range from 2 to 9 in some cases. There-

fore selecting only one of them through `Method 2` implies that the values from the remaining cells are ignored, hence it results in an under-sampling that is evident for the CWENO 5th-order method with low central stencil weight.

It can be summarised with a great degree of confidence that if the FFT process involves either under-sampling due to the type of mesh involved and the method chosen (e.g. `Method 2`) or oversampling and projection similar to `Method 3`, then at high-wave numbers the expected dissipation due to the grid-resolution is not manifested as expected and as seen in hexahedral mesh. On the contrary, it is expressed by a tail-off before the grid-size limit which is more pronounced with `Method 3` on prismatic and uniform tetrahedral mesh, and more pronounced with `Method 2` on the arbitrary tetrahedral mesh. On the other hand the filtering/averaging ingredient of `Method 1`, consistently exhibits the same behaviour where its dissipative nature is dependent on the number of elements that are contained within each control volume of the ASM cells, and therefore the filtering is the most excessive in the tetrahedral meshes followed by the prismatic mesh.

In particular, the hexahedral mesh is the most sensitive to the choice of linear weight, followed by the prismatic mesh and the tetrahedral mesh which is the least sensitive, and this is due to the increased numerical dissipation at low-Mach number regions for multidimensional reconstructions. The 3D energy spectra can complement the calibration of several numerical methods intended for iLES, towards providing the right amount of dissipation for restoring the physical consistency [3,10,35].

5. Conclusions

For a numerical scheme to be suitable for iLES, it should exhibit just the “right” amount of dissipation, across all the wave numbers and during the entire simulation. For this reason, the presented methods could prove a useful tool for calibrating these schemes. Unfortunately due to the non-uniform data associated with unstructured meshes, several approximations are required to perform a 3D FFT for the energy spectra of turbulent flow simulations in a way that we can understand the performance of several schemes. When realizing the differences across the different schemes, and pursuing improvements for their dissipation/dispersion characteristics, it is of paramount importance to understand the underlying approximations used for the method employed for the 3D FFT, otherwise, we might be driven to the wrong conclusions. The presented methods highlight this last argument. This is particularly important for tuning and calibrating high-order non-linear schemes for unstructured meshes where the dissipation can be adjusted based on the cell-local kinetic energy dissipation rate as previously documented in [4], an approach we plan to further investigate in the context of unstructured methods.

CRediT authorship contribution statement

Panagiotis Tsoutsanis: Conceptualization, Formal analysis, Funding acquisition, Methodology, Resources, Software, Visualization, Writing – original draft, Writing – review & editing. **Xesus Nogueira:** Conceptualization, Formal analysis, Funding acquisition, Methodology, Resources, Software, Visualization, Writing – review & editing. **Lin Fu:** Conceptualization, Formal analysis, Funding acquisition, Methodology, Resources, Visualization, Writing – review & editing.

Declaration of competing interest

Declaration of interest: none.

Data availability

The datasets of the test problems in this article are available at the Cranfield Online Research Data repository https://doi.org/10.17862/cranfield.rd.21271122.

Acknowledgements

The authors acknowledge the computing time on ARCHER2 through UK Turbulence Consortium [EPSRC grant number EP/L000261/1 and EP/R029326/1]. P. Tsoutsanis also acknowledges the support provided by the EPSRC grant for “Adaptively Tuned High-Order Unstructured Finite-Volume Methods for Turbulent Flows” [EPSRC grant number EP/W037092/1]. X. Nogueira also acknowledges the support provided by FEDER funds of the European Union through the Ministerio de Ciencia e Innovación of the Spanish Government [Grant PID2021-125447OB-I00], and [Grant TED2021-129805B-I00]. L. Fu acknowledges the fund from the Research Grants Council (RGC) of the Government of Hong Kong Special Administrative Region (HKSAR) with RGC/ECS Project (No. 26200222) and the fund from Guangdong Basic and Applied Basic Research Foundation (No. 2022A1515011779).

References

[1] R. Moura, G. Mengaldo, J. Peiro, S. Sherwin, On the eddy-resolving capability of high-order discontinuous Galerkin approaches to implicit LES / under-resolved DNS of Euler turbulence, J. Comput. Phys. 330 (2017) 615–623, https://doi.org/10.1016/j.jcp.2016.10.056.

[2] D. Fauconnier, C. De Langhe, E. Dick, Construction of explicit and implicit dynamic finite difference schemes and application to the large-eddy simulation of the Taylor-Green vortex, J. Comput. Phys. 228 (21) (2009) 8053–8084.
[3] S. Hickel, N. Adams, J. Domaradzki, Letter to the editor: on the evolution of dissipation rate and resolved kinetic energy in ALDM simulations of the Taylor-Green flow, J. Comput. Phys. 229 (6) (2010) 2422–2423.
[4] J. Fernandez Fidalgo, L. Ramirez, P. Tsoutsanis, I. Colominas, X. Nogueira, A reduced-dissipation WENO scheme with automatic dissipation adjustment, J. Comput. Phys. 425 (2021), https://doi.org/10.1016/j.jcp.2020.109749.
[5] M. Tavelli, M. Dumbser, A pressure-based semi-implicit space-time discontinuous Galerkin method on staggered unstructured meshes for the solution of the compressible Navier-Stokes equations at all Mach numbers, J. Comput. Phys. 341 (2017) 341–376.
[6] D. Drikakis, C. Fureby, F. Grinstein, D. Youngs, Simulation of transition and turbulence decay in the Taylor-Green vortex, J. Turbul. 8 (2007) 1–12.
[7] L. Fu, X.Y. Hu, N.A. Adams, A family of high-order targeted ENO schemes for compressible-fluid simulations, J. Comput. Phys. 305 (2016) 333–359.
[8] L. Fu, X. Hu, N. Adams, Targeted ENO schemes with tailored resolution property for hyperbolic conservation laws, J. Comput. Phys. 349 (2017) 97–121, https://doi.org/10.1016/j.jcp.2017.07.054.
[9] P. Tsoutsanis, M. Dumbser, Arbitrary high order central non-oscillatory schemes on mixed-element unstructured meshes, Comput. Fluids 225 (2021), https://doi.org/10.1016/j.compfluid.2021.104961.
[10] P. Tsoutsanis, A. Antoniadis, K. Jenkins, Improvement of the computational performance of a parallel unstructured WENO finite volume CFD code for implicit large eddy simulation, Comput. Fluids 173 (2018) 157–170, https://doi.org/10.1016/j.compfluid.2018.03.012.
[11] B. Vermeire, F. Witherden, P. Vincent, On the utility of gpu accelerated high-order methods for unsteady flow simulations: a comparison with industry-standard tools, J. Comput. Phys. 334 (2017) 497–521, https://doi.org/10.1016/j.jcp.2016.12.049.
[12] Z. Ji, T. Liang, L. Fu, A class of new high-order finite-volume TENO schemes for hyperbolic conservation laws with unstructured meshes, J. Sci. Comput. 92 (61) (2022), https://doi.org/10.1007/s10915-022-01925-5.
[13] A. Barnett, J. Magland, L. Klinteberg, A parallel nonuniform fast Fourier transform library based on an "exponential of semicircle" kernel, SIAM J. Sci. Comput. 41 (5) (2019) C479–C504, https://doi.org/10.1137/18M120885X.
[14] UCNS3D CFD code, http://www.ucns3d.com. (Accessed 10 October 2022).
[15] A.F. Antoniadis, D. Drikakis, P.S. Farmakis, L. Fu, I. Kokkinakis, X. Nogueira, P.A. Silva, M. Skote, V. Titarev, P. Tsoutsanis, Ucns3d: an open-source high-order finite-volume unstructured cfd solver, Comput. Phys. Commun. 279 (2022) 108453, https://doi.org/10.1016/j.cpc.2022.108453.
[16] P. Tsoutsanis, V. Titarev, D. Drikakis, WENO schemes on arbitrary mixed-element unstructured meshes in three space dimensions, J. Comput. Phys. 230 (4) (2011) 1585–1601.
[17] P. Tsoutsanis, A. Antoniadis, D. Drikakis, WENO schemes on arbitrary unstructured meshes for laminar, transitional and turbulent flows, J. Comput. Phys. 256 (2014) 254–276.
[18] E. Toro, M. Spruce, W. Speares, Restoration of the contact surface in the HLL-Riemann solver, Shock Waves 4 (1) (1994) 25–34.
[19] R.J. Spiteri, S.J. Ruuth, A new class of optimal high-order strong-stability-preserving time-stepping schemes, SIAM J. Numer. Anal. 40 (2) (2002) 469–491.
[20] P. Tsoutsanis, D. Drikakis, A high-order finite-volume method for atmospheric flows on unstructured grids, J. Coupled Syst. Multiscale Dyn. 4 (2016) 170–186, https://doi.org/10.1166/jcsmd.2016.1104.
[21] A. Antoniadis, P. Tsoutsanis, D. Drikakis, Numerical accuracy in RANS computations of high-lift multi-element airfoil and aircraft configurations, in: 53rd AIAA Aerospace Sciences Meeting, vol. 0317, 2015.
[22] A. Antoniadis, P. Tsoutsanis, D. Drikakis, High-order schemes on mixed-element unstructured grids for aerodynamic flows, in: 42nd AIAA Fluid Dynamics Conference and Exhibit, vol. 2833, 2012.
[23] P. Tsoutsanis, I. Kokkinakis, L. Konozsy, D. Drikakis, R. Williams, D. Youngs, Comparison of structured- and unstructured-grid, compressible and incompressible methods using the vortex pairing problem, Comput. Methods Appl. Mech. Eng. 293 (2015) 207–231, https://doi.org/10.1016/j.cma.2015.04.010.
[24] P. Farmakis, P. Tsoutsanis, X. Nogueira, WENO schemes on unstructured meshes using a relaxed a posteriori MOOD limiting approach, Comput. Methods Appl. Mech. Eng. 363 (2020), https://doi.org/10.1016/j.cma.2020.112921.
[25] P. Tsoutsanis, Extended bounds limiter for high-order finite-volume schemes on unstructured meshes, J. Comput. Phys. 362 (2018) 69–94.
[26] N. Simmonds, P. Tsoutsanis, A. Antoniadis, K. Jenkins, A. Gaylard, Low-Mach number treatment for finite-volume schemes on unstructured meshes, Appl. Math. Comput. 336 (2018) 368–393.
[27] F. Ricci, P. Silva, P. Tsoutsanis, A. Antoniadis, Hovering rotor solutions by high-order methods on unstructured grids, Aerosp. Sci. Technol. 97 (2020), https://doi.org/10.1016/j.ast.2019.105648.
[28] P. Silva, P. Tsoutsanis, A. Antoniadis, Simple multiple reference frame for high-order solution of hovering rotors with and without ground effect, Aerosp. Sci. Technol. 111 (2021), https://doi.org/10.1016/j.ast.2021.106518.
[29] P. Tsoutsanis, Knl performance comparison UCNS3D, ARCHER performance report, 2017, pp. 157–170, www.archer.ac.uk/community/benchmarks/archer-knl/KNLperfUCNS3D.pdf.
[30] S.B. Pope, Turbulent Flows, Cambridge University Press, 2000.
[31] P. Tsoutsanis, Stencil selection algorithms for WENO schemes on unstructured meshes, J. Comput. Phys. X 4 (2019), https://doi.org/10.1016/j.jcpx.2019.100037.
[32] A.H. Barnett, Non-uniform Fast Fourier Transform Library of Types 1, 2, 3 in Dimensions 1, 2, 3 [online] 2022, v2.1.0 [cited 12 July 2022].
[33] J. Bull, A. Jameson, Simulation of the Taylor-Green vortex using high-order flux reconstruction schemes, AIAA J. 53 (9) (2015) 2750–2761.
[34] C.-W. Shu, W.-S. Don, D. Gottlieb, O. Schilling, L. Jameson, Numerical convergence study of nearly incompressible, inviscid Taylor-Green vortex flow, J. Sci. Comput. 24 (1) (2005) 569–595.
[35] L. Fu, X. Hu, N.A. Adams, A targeted ENO scheme as implicit model for turbulent and genuine subgrid scales, Commun. Comput. Phys. 26 (2) (2019) 311–345.
[36] F. Fambri, M. Dumbser, Spectral semi-implicit and space-time discontinuous Galerkin methods for the incompressible Navier-Stokes equations on staggered Cartesian grids, Appl. Numer. Math. 110 (2016) 41–74.
[37] H. Luo, Y. Xia, S. Spiegel, R. Nourgaliev, Z. Jiang, A reconstructed discontinuous Galerkin method based on a hierarchical weno reconstruction for compressible flows on tetrahedral grids, J. Comput. Phys. 236 (1) (2013) 477–492, https://doi.org/10.1016/j.jcp.2012.11.026.
[38] J. Zhu, X. Zhong, C.-W. Shu, J. Qiu, Runge-Kutta discontinuous Galerkin method using a new type of weno limiters on unstructured meshes, J. Comput. Phys. 248 (2013) 200–220, https://doi.org/10.1016/j.jcp.2013.04.012.
[39] H. Luo, J. Baum, R. Lohner, A Hermite weno-based limiter for discontinuous Galerkin method on unstructured grids, J. Comput. Phys. 225 (1) (2007) 686–713, https://doi.org/10.1016/j.jcp.2006.12.017.
[40] M. Dumbser, M. Kaser, V. Titarev, E. Toro, Quadrature-free non-oscillatory finite volume schemes on unstructured meshes for nonlinear hyperbolic systems, J. Comput. Phys. 226 (1) (2007) 204–243, https://doi.org/10.1016/j.jcp.2007.04.004.
[41] M. Dumbser, M. Kaser, Arbitrary high order non-oscillatory finite volume schemes on unstructured meshes for linear hyperbolic systems, J. Comput. Phys. 221 (2) (2007) 693–723, https://doi.org/10.1016/j.jcp.2006.06.043.
[42] M. Dumbser, D. Balsara, E. Toro, C.-D. Munz, A unified framework for the construction of one-step finite volume and discontinuous Galerkin schemes on unstructured meshes, J. Comput. Phys. 227 (18) (2008) 8209–8253, https://doi.org/10.1016/j.jcp.2008.05.025.
[43] P. Tsoutsanis, M.S.S. Pavan Kumar, P.S. Farmakis, A relaxed a posteriori mood algorithm for multicomponent compressible flows using high-order finite-volume methods on unstructured meshes, Appl. Math. Comput. 437 (2023) 127544, https://doi.org/10.1016/j.amc.2022.127544.

[44] M. Brachet, D. Meiron, B. Nickel, R. Morf, U. Frisch, S. Orszag, Small-scale structure of the Taylor-Green vortex, J. Fluid Mech. 130 (1983) 411–452, https://doi.org/10.1017/S0022112083001159.
[45] J. Ruano, A. Baez Vidal, J. Rigola, F.X. Trias, A new general method to compute dispersion errors on Cartesian stretched meshes for both linear and non-linear operators, Comput. Phys. Commun. 271 (2022) 108192, https://doi.org/10.1016/j.cpc.2021.108192.